Carbon 219 (2024) 118799

Contents lists available at ScienceDirect

Carbon

journal homepage: www.elsevier.com/locate/carbon

Disentangling the self-diffusional dynamics of H_2 adsorbed in micro- and mesoporous carbide-derived carbon by wide temporal range quasi-elastic neutron scattering

Miriam Koppel [a], Rasmus Palm [a,b,*], Riinu Härmas [a], Mark Telling [c], Manh Duc Le [c], Tatiana Guidi [c,d], Kenneth Tuul [a], Maarja Paalo [a], Laura Kalder [a], Jacek Jagiello [e,g], Tavo Romann [a], Jaan Aruväli [f], Martin Månsson [b], Enn Lust [a]

[a] Institute of Chemistry, University of Tartu, Ravila 14a, 50411, Tartu, Estonia
[b] Department of Applied Physics, KTH Royal Institute of Technology, SE-106 91, Stockholm, Sweden
[c] ISIS Neutron and Muon Facility, STFC Rutherford Appleton Laboratory, Chilton, Didcot, OX11 0QX, United Kingdom
[d] School of Science and Technology, Physics Division, University of Camerino, I-62032, Camerino, Italy
[e] Micromeritics Instrument Corporation, 4356 Communications Dr, Norcross, GA, 30093, United States
[f] Institute of Ecology and Earth Sciences, University of Tartu, Ravila 14a, 50411, Tartu, Estonia
[g] AGH University of Science and Technology, Faculty of Energy and Fuels, al. A. Mickiewicza 30, 30-059 Kraków, Poland

ARTICLE INFO

Keywords:
H_2 adsorption
H_2 self-diffusion
Carbide-derived carbon
Quasi-elastic neutron scattering
Ultramicroporous confinement

ABSTRACT

Understanding the processes guiding the confinement of adsorbed H_2 in different porous structures is vital for the development of adsorbents for effective cryo-adsorptive H_2 storage systems. Quasi-elastic neutron scattering (QENS) is applied over a wide range of timescales (0.2 ps – 150 ps) to determine different self-diffusion mechanisms of H_2 adsorbed in a carbide (synthesized from TiC via the sol-gel method) derived carbon (sol-gel TiC-CDC) adsorbent with hierarchical porous structure. The bulk and porous structure is characterized by gas adsorption, Raman spectroscopy, and wide-angle X-ray scattering methods. Sol-gel TiC-CDC belongs to a series of CDCs that have been previously characterized and where the self-diffusion of adsorbed H_2 has been investigated with QENS. Sol-gel TiC-CDC is very mesoporous, has relatively high stacking (2.76 graphenic layers per stack), and small interlayer spacing of graphenic sheets (3.43 Å) in comparison to other CDCs in the series, thus, being a well-ordered highly porous CDC. Restricted rotational self-diffusion of adsorbed H_2 is determined in ultra-micropores (pore width, w, < 7 Å) and translationally self-diffusing H_2 adsorbed in multilayers across multiple timescales are determined in micro- and mesopores (7 Å $< w < 500$ Å). The microporous and graphenic structure of the CDC does not remarkably affect the self-diffusion of H_2 at high surface coverages. The simultaneous determination of adsorbed H_2 motions across different timescales allows to analyze the influence of micro- and mesopores under H_2 loading conditions, which are close to the ones used in technical applications and are vital for adsorbent optimization.

1. Introduction

The confinement and self-diffusion of H_2 adsorbed in porous materials is of interest for both fundamental and applicational purposes, such as isotope separation, H_2 storage via physisorption, and catalysis [1–3]. Currently, the high cost of H_2 storage is one of the greatest obstacles to realizing a sustainable society based on H_2 as an energy carrier [4]. Namely, H_2 needs to be stored either at a high pressure of 300 bar – 700 bar or at a very low temperature of 20 K to increase the volumetric and gravimetric density of H_2 [5]. Porous materials have attracted interest as H_2 storage materials since these can help to decrease the storing pressure and increase the storing temperature of H_2. The optimal conditions for using porous materials for H_2 storage are in the temperature range of 77 K – 150 K and the storage pressure as low as ~250 bar [6]. The porous structure of the carbon adsorbent has been shown to have a great impact on H_2 storage properties, e.g., H_2 uptake and the self-diffusion rate [1].

When H_2 is adsorbed in pores with widths, w, $< \sim 4$ Å, where w is the effective distance between the pore walls obtained by gas adsorption

* Corresponding author. Institute of Chemistry, University of Tartu, Ravila 14a, 50411, Tartu, Estonia.
E-mail address: rasmus.palm@ut.ee (R. Palm).

https://doi.org/10.1016/j.carbon.2024.118799
Received 5 November 2023; Received in revised form 24 December 2023; Accepted 5 January 2024
Available online 6 January 2024

analysis, only one layer of adsorbed H_2 can be accommodated between the carbon layers [7]. The lowest accessible pore w is defined by the kinetic diameter 2.9 Å of the H_2 molecule. The electrostatic repulsion of the electron shells between the pore wall and the H_2 molecule start impeding entry of the H_2 molecule in case of pores just slightly larger than the H_2 molecule (e.g., $w \leq \sim 3$ Å) [8]. The adsorbed phase of H_2 formed in ultramicropores, i.e., pores with $w < 7$ Å, has been shown to be denser than liquid H_2 at 77 K due to the attractive forces between the H_2 molecules and the adsorbent pore walls [9–11], resulting in highly restricted self-diffusion of H_2 at low temperatures ($\leq$ 40 K) [12]. The occurrence of H_2 adsorption of at least two layers (in pores with $w \geq \sim 7$ Å) has been predicted theoretically [7] and the maximal H_2 storage density in case of pores with widths 6 Å – 7 Å has been shown by both theoretical and experimental methods [1,12–22].

For pores with $w \geq \sim 10$ Å, the influence of the electrostatic field of the opposite pore walls on the adsorbed H_2 is negligible [15]. Therefore, opposite pore walls can be regarded as two independent surfaces for adsorbing H_2. If the pores are even larger, i.e., $w \geq 20$ Å, additional H_2 layers on top of the H_2 monolayer can be present in the adsorbed phase. These additional layers are not in direct contact with the pore wall and multiple H_2 layers form which are difficult to distinguish [7,23]. The self-diffusion of these H_2 layers adsorbed on top of the H_2 monolayer in these pores can be much faster compared to the self-diffusion in the adsorbed monolayer and/or H_2 adsorbed in ultramicropores. As a result, self-diffusion over multiple timescales can occur [13,24–26].

Carbide-derived carbons (CDCs) have shown excellent performance in many applications, such as electrode materials in supercapacitors and polymer electrolyte membrane fuel cells, and as adsorbents for H_2 storage applications [27–32]. The porous structure of the CDC can vary from very ultramicroporous to mainly meso- and macroporous, their surface area can vary from relatively low (e.g., 146 $m^2\ g^{-1}$) [33] to beyond the theoretical maximum 2600 $m^2\ g^{-1}$ of an infinite sheet of graphene [34], and their pore size distribution can vary from single modal to trimodal [35–39]. The graphene-like platelet size of CDCs has been shown to vary from 23 Å to 82 Å, and the interlayer distance of the graphene-like sheets has been shown to be as large as 4.53 Å [40]. The mesopores of the CDCs can be differently shaped, e.g., spherical, cylindrical, and slit-like [41,42] and the micro- and mesopores can have different levels of pore wall corrugation (i.e., volume of ultramicropores) [13]. Their diverse and tunable porous and bulk structure makes them perfect model materials for studying the different types of self-diffusion processes of adsorbed H_2.

Quasi-elastic neutron scattering (QENS) is a well-suited method for investigating self-diffusion of adsorbed H_2 since H_2 has a large incoherent neutron scattering cross-section and the neutron energies used are unique for probing motion on timescales characteristic to diffusional processes [43,44]. It has been shown with QENS that H_2 adsorbed in different adsorbents, e.g., CDCs, zeolites, exfoliated graphite, and micro- and mesoporous carbons self-diffuses on distinguishable timescales [13,24–26,45]. However, it should be noted that fast H_2 mobility arising at high H_2 loading conditions is difficult to quantify since considerable amounts of H_2 interact weakly with the absorbent and self-diffuses with virtually no restrictions. As a result a broad, background-like, quasi-elastic scattering signal (i.e., with quasi-elastic broadening $\geq$ 2 meV) is observed which is usually beyond the time resolution of the neutron instrument used [13]. The fast H_2 components adsorbed in mesoporous carbon and exfoliated graphite have been shown to self-diffuse translationally with residency times between translational jumps in the range from ~0.1 ps to ~2 ps at temperatures from 12 K to 80 K [45]. The more restricted H_2 component has been shown to self-diffuse rotationally with residency times between rotational jumps in the range from 0.3 ps to 0.8 ps at temperatures from 22 K to 80 K [45]. In addition, the strongly confined H_2 adsorbed in a zeolite has been shown to self-diffuse translationally with a ~11 ps residency time between translational jumps at 50 K, i.e., the presence of very restricted self-diffusion of adsorbed H_2 in micropores of a zeolite material [25]. Some of the adsorbed H_2 can be so restricted that a phase as dense as, or even denser than liquid H_2 forms and, thus, H_2 self-diffuses too slowly to be investigated with the QENS method [12,13]. However, the self-diffusion of H_2 adsorbed in an ultramicroporous carbon has been analyzed at temperatures as low as 22 K with a QENS instrument set up to detect very slow dynamics [16,45].

In this work, CDC obtained from TiC synthesized using the sol-gel method (denoted as sol-gel TiC-CDC) is used to simultaneously study different H_2 self-diffusional motions present in a micro- and mesoporous model carbon material. Sol-gel TiC-CDC is a highly promising electrode material for energy storage applications due to its chemical stability and highly porous structure [37,46]. The porous structure of sol-gel TiC-CDC is determined from N_2, CO_2, and H_2 adsorption data; the isotherms are used simultaneously to model the pore size distribution [47,48]. The use of multiple adsorbing gases, including H_2, gives a more realistic picture of the porous structure in the w range up to 500 Å and, thus, enables micro- and ultramicropores to be differentiated with greater reliability [47,48]. The algorithm derived by Ruland and Smarsly on the wide-angle X-ray scattering (WAXS) data and Raman spectra is used to characterize the graphenic structure (defined as in Ref. [49]) of sol-gel TiC-CDC [50,51]. This enables the structural parameters of the carbon to be estimated quantitatively, e.g., average layer stacking size and average graphene-like layer extent [50,51]. The sol-gel TiC-CDC adsorbent presented here belongs to a larger group of CDCs that have been characterized thoroughly [40] and in which the self-diffusion of adsorbed H_2 has been studied with QENS [12–14].

In this work, the different modes of self-diffusion of H_2 absorbed in the pores of sol-gel TiC-CDC are studied *in situ* using the QENS method over a wide range of experimental timescales (~0.2 ps – 150 ps timescale). This temporal range is achieved by collating data collected using the neutron instruments IRIS [52] and MARI [53] (at the ISIS pulsed neutron and muon source). While each instrument allows access to different temporal and spatial regimes, the data itself is collected with the samples under common temperature (10 K – 100 K) and H_2 loading pressure (~0.01 bar – 1 bar) conditions. As a result, a more detailed view of the different motions of H_2 adsorbed in a micro- and mesoporous carbon adsorbent is obtained.

2. Methods

2.1. Synthesis and physical characterization

2.1.1. Synthesis

The sol-gel synthesis method was used to prepare TiC, with chlorination being used to synthesize the carbon sample used for the experiment (from here on referred to as sol-gel TiC-CDC). The synthesis process is described in detail in Ref. [38] and the synthesis route is briefly summarized in Fig. 1.

2.1.2. Gas adsorption

N_2, CO_2, and H_2 adsorption isotherms of the sol-gel TiC-CDC sample were measured using an ASAP2020 (Micromeritics, USA) adsorption analyzer at 77 K, 273 K, and 77 K, respectively. The sample were outgassed at 300 °C and at a vacuum of at least 13 μbar for 12 h before the adsorption measurements.

The pore size distribution (PSD) was obtained by applying the two-dimensional non-local density functional theory model for carbon materials with heterogeneous surfaces (2D-NLDFT-HS), using the SAIEUS (Micromeritics, USA) software (developmental version) [54] simultaneously to the N_2, CO_2, and H_2 adsorption isotherm data. 2D-NLDFT-HS model based specific surface area, S_{DFT}, and volume of pores, V_{DFT}, were obtained. The volume of the ultramicropores, V_{ump}, the volume of the micropores, V_{micro}, and the volume of the mesopores, V_{meso}, are calculated from the cumulative pore volume (Fig. S1 in SI section 1) in the range $w < 7$ Å, $w < 20$ Å, and 20 Å $< w <$ 500 Å, respectively. The surface area, S_{BET}, calculated from the Brunauer-Emmett-Teller method

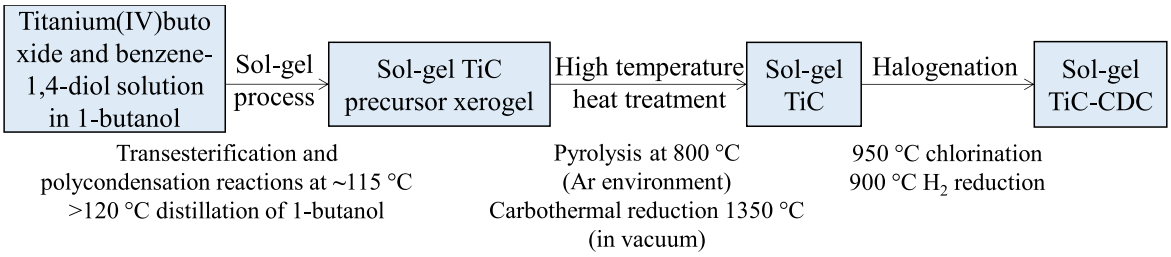

Fig. 1. Synthesis routine for sol-gel TiC-CDC. (A colour version of this figure can be viewed online.)

as applied to N_2 adsorption data at 77 K in the p/p_0 range from 0.05 to 0.2, and the total pore, V_{tot}, value calculated from N_2 adsorption data at 77 K and at $p/p_0 = 0.95$, can be seen in supplementary information (SI) section 1 in Table S1.

2.1.3. Raman spectroscopy

Raman spectra were obtained with an inVia micro-Raman spectrometer (Renishaw, Kingswood, UK) at an excitation wavelength of 514 nm. The Raman spectrum presented, and analyzed, was chosen from a set of four measurements from different sample spots and assumed to be a representative average of the sample. The first-order Raman spectra was fitted with 4 Lorentzian and 1 Gaussian peak functions to separate the D_S, D_A, G_S, G_A, and D′ bands (L + L + G + L + L, respectively) (Fig. S2 in SI section 2). These have been shown to be characteristic of non-graphitic carbon materials [55,56] and the fitting results can be seen in SI Table S2 in section 2. This fitting process has been shown to be suitable for CDCs [40], deconvoluting bands in a consistent and comparable manner between various carbonaceous materials, and yielded a good deconvolution for the sol-gel TiC-CDC under study (Fig. S2 in SI section 2). Both D_S and D_A are contributions of the D-band and both of the G_S and G_A are contributions of the G-band, respectively; with the S bands originating from vibrations near crystallite edge-areas or near defects. The A bands originate from vibrations inside the graphene-like platelets [54]. The D′-band is a disorder-induced contribution to the D-band [56,57].

Characteristic properties, such as integrated intensities and widths of the D- and G-bands, the integrated intensity ratio, $I_{\Sigma D}/I_{\Sigma G}$ (Eq. (1)), and the full width at half maximum of the D-band ($FWHM_{DA}$) yield insight into the relative structural order of a carbon material [40,55–57].

$$\frac{I_D}{I_G} = \frac{A_D^S + A_D^A}{A_G^S + A_G^A + A_{D'}} \quad (1)$$

Here, A_i is the integrated intensity of the associated deconvoluted band *i*.

2.1.4. Wide-angle X-ray scattering

A wide-angle X-ray scattering pattern of the sol-gel TiC-CDC sample was obtained using a D8 Advance (Bruker, Germany) diffractometer; Cu Kα radiation of wavelength 1.5406 Å. The scattering pattern was measured in the 2θ range from 13° to 80° with a counting time of 166 s per step and a step size of 0.0128° using a LynxEye detector. Fitting of the diffractogram is performed across the full measured 2θ range with CarbX software (Fig. S3 in SI section 3), resulting in 14 inter- and intralayer parameters (Table S3 in SI section 3) [50,51]. The average graphene-like platelet size, L_a, the average stacking size, L_c, the average interlayer spacing, a_3, and the average number of graphene-like layers per stack, $\langle N \rangle$ (which is calculated as $\langle N \rangle = \frac{L_c}{a_3(1+\kappa_c)}$, where κ_c is the polydispersity of the stack height) are of main interest for the characterization of the level of ordering of the graphenic domains in sol-gel TiC-CDC [51].

2.2. Quasi-elastic neutron scattering

Neutron scattering experiments were performed at the ISIS pulsed neutron and muon source, UK, using the MARI [53] and IRIS [52] spectrometers. The data can be accessed at Refs [58,59]. The sample was outgassed at 300 °C to remove air moisture and other adsorbed species and was transferred to an annular cylindrical aluminum sample can. The sample thickness of 0.2 mm was chosen such that the transmission would be more than 90%. At this level, multiple scattering effects can be considered negligible.

The measurement processes were identical for experiments on both the MARI and IRIS spectrometers and analogous to the experiments performed in Refs. [12,13]. The sample was cooled using a helium cryostat and, for dosing H_2, the gas handling system can be seen in SI Figure S4 in section 4. First, the signal from the outgassed carbon sample was measured in the temperature range from 20 K to 100 K. Thereafter, the samples were cooled down to 77 K and dosed in turn to establish three different H_2 loading pressures, $p_{H2,load}$, - 14 mbar, 225 mbar, and 969 mbar – which resulted in the values of the total amount of H_2 per 1 g of sol-gel TiC-CDC in the closed sample cell (n_{H2}) of 1.7 mmol g^{-1}, 10 mmol g^{-1}, and 31 mmol g^{-1}. These n_{H2} values were chosen to ensure the surface coverage of 30%, 130%, and 290% at 20 K (Table S7 in SI section 4). A surface coverage over 100% means that the monolayer of H_2 is filled and some of the H_2 is adsorbed in subsequent layers on top of the monolayer. The loading pressures for the experiment on MARI and on IRIS were calculated so that the surface coverage would be equivalent in both experiments. The exact H_2 loading pressures and calculations are in SI section 4.

After establishing adsorption equilibrium over approximately 1 h, the sample holder was hermetically sealed from the gas handling system (Fig. S4) and neutron scattering data from the sample with the adsorbed H_2 was collected in the temperature range from 10 K to 100 K. The neutron scattering data obtained at the lowest temperature (10 K for IRIS and 20 K for MARI) and at $n_{H2} = 1.7$ mmol g^{-1} was used for instrument calibration and resolution purposes during subsequent data analysis. At these lowest applied *T* and n_{H2} conditions, the H_2 present in the sol-gel TiC-CDC could be presumed static, i.e., frozen solid in the pores, at least on the experimental time scales afforded by the used neutron instrumental set-up (Table 1). The H_2 pressure in the sample cell was monitored (SI Table S5 section 4) and used to calculate the sample surface coverages and pore volume occupancies at all conditions throughout both experiments (more details in SI section 4).

The energy resolution, momentum transfer, and temporal and spatial range configurations used on the IRIS and MARI spectrometers are summarized in Table 1. For IRIS, the neutron scattering data were collected with the spectrometer configured to energy analyze the

Table 1
The characteristics of the IRIS and MARI instruments and configurations used.

	Energy resolution meV	Temporal range ps	*Q*-range Å^{-1}	Spatial range Å
IRIS (PG002)	0.0175	5–150	0.42–1.85	3–15
MARI	0.43	0.2–10	0.4–6*	1–16

*The analyzable *Q* range is truncated at Q_{max} ~1.8 Å^{-1}.

scattered neutron beam using the 002 graphite (PG002) analyzer reflection. The Q-range used for analysis, from both IRIS and MARI, was truncated at Q_{max} ~1.8 Å^{-1}. The Q-range was truncated because of the strong coherent scattering signal arising from the graphenic carbon (002) diffraction peak above $Q \sim 1.8$ Å^{-1}; this signal greatly contaminated the measured data (Fig. S6 in SI section 5).

On IRIS, the scattered neutrons were detected in the energy transfer range from −0.3 meV to 1.2 meV, where negative energy transfer means that neutrons gained energy during the scattering process and positive energy transfer means that neutrons lost energy during the scattering process. The reduced data were collated in the Q range of 0.42 Å^{-1} - 1.8 Å^{-1} into five distinct Q groups/values at $n_{H2} = 1.7$ mmol g^{-1} and nine Q groups at $n_{H2} \geq 10$ mmol g^{-1}. On MARI spectrometer, the neutrons were detected in the energy transfer range from −20 meV to 20 meV. The reduced data were collated in the Q range of 0.4 Å^{-1} - 1.8 Å^{-1} into nine Q groups at $n_{H2} \geq 10$ mmol g^{-1} to match the Q grouping of the scattering data from IRIS. The data reduction and analysis for both experiments was carried out using Mantid [60] and OriginLab 2016 (OriginLab Corporation) softwares.

To deconvolve the different spectral contribution to each measured neutron scattering spectrum, $S(Q,E)$, the data was fit with functional form comprised of: elastic and quasi-elastic components, an instrumental resolution function, and a constant baseline (Eq. (2)):

$$S(Q,E) = \left[A_0(Q)\delta(E) + \sum_i^n A_i(Q)L(E,\Gamma_i)\right] \otimes R(Q,E) + y_0 \quad (2)$$

Here, $S(Q,E)$ is the dynamical structure factor, Q is the scattering vector value, E is the energy transfer, $\delta(E)$ is the Dirac delta function describing the elastic scattering, $A_0(Q)$ and $A_1(Q)$ are the fractions of elastic and quasi-elastic scattering signals, n is the number of quasi-elastic components, $L(E, \Gamma_i)$ is the Lorentzian function which describes mathematically the quasi-elastic component, Γ is the half-width at half maximum (HWHM) of the quasi-elastic component, $R(Q,E)$ in the instrumental resolution function, and y_0 is the baseline.

In total, four different quasi-elastic components, i.e. four different H_2 self-diffusional dynamics, denoted with L_1, L_2, $L_{3.10}$ and $L_{3.31}$ are distinguished and analyzed (Fig. 2). The subscripts 10 and 31 in $L_{3.10}$ and $L_{3.31}$, respectively, denote the values of total amount of H_2 per 1 g of sol-gel TiC-CDC in the closed sample cell in mmol g^{-1} at which the width of the quasi-elastic component is determined. The $S(Q,E)$ obtained on IRIS at $n_{H2} = 1.7$ mmol g^{-1} are fitted with Eq. (2) using one Lorentzian function – L_1. The $S(Q,E)$ obtained on IRIS at $n_{H2} = 10$ mmol g^{-1} are fitted with Eq. (2) using two Lorentzian functions – L_1 predetermined at $n_{H2} = 1.7$ mmol g^{-1} and freely fitted L_2. The $S(Q,E)$ obtained on MARI at $n_{H2} \geq 10$ mmol g^{-1} are fitted with Eq. (2) using two Lorentzian functions accounting for two quasi-elastic broadenings – L_2 predetermined at $n_{H2} = 10$ mmol g^{-1} obtained from data measured on IRIS $S(Q,E)$ and freely fitted $L_{3.10}$. MARI and IRIS spectrometers have an overlap in the temporal range where H_2 motions described with L_2 take place (Fig. 2).

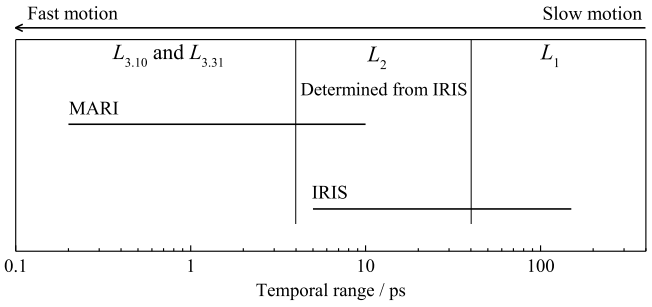

Fig. 2. Schematics of H_2 components analyzable in the temporal ranges of MARI and IRIS spectrometers. (A colour version of this figure can be viewed online.)

Thus, the L_2 component is fixed based on the results obtained at $n_{H2} = 10$ mmol g^{-1} from the data obtained on the IRIS spectrometer to account for the slower motions probed with MARI, revealing a more reliable broader Lorentzian (L_3). The motions of H_2 component described with L_3 have a clear difference in linewidths at $n_{H2} = 10$ mmol g^{-1} and at $n_{H2} = 31$ mmol g^{-1} and are denoted with $L_{3.10}$ at $n_{H2} = 10$ mmol g^{-1} and $L_{3.31}$ at $n_{H2} = 31$ mmol g^{-1}, respectively. Linewidths of the L_2 component are kept constant at $n_{H2} \geq 10$ mmol g^{-1} as they stayed equal within the uncertainty margins at $n_{H2} \geq 10$ mmol g^{-1}. Similarly, in a previous QENS experiment with H_2 adsorbed in Mo_2C-CDC samples on the NEAT spectrometer, the linewidths of the narrower component stayed equal within the uncertainty margins over n_{H2} values (SI of Ref [13]). The fitting of the $S(Q,E)$ can be seen in SI in section 6 in Figs. S8–S13.

3. Results and discussion

3.1. Physical characterization

The pore size distribution (PSD) for sol-gel TiC-CDC has been previously calculated using N_2 and CO_2 adsorption data fitted with the 2D-NLDFT-HS model. This analysis revealed that the adsorbent exhibits both micro- and mesopores, where the mesoporosity originates from the precursor TiC sol-gel synthesis process [38]. In this work, the N_2, CO_2, and H_2 adsorption isotherms have been globally fitted using the 2D-NLDFT-HS model (Fig. 3a–c) to calculate the PSD of sol-gel TiC-CDC (Fig. 3d, Fig. S1). The addition of the H_2 isotherm data to the PSD calculation resulted in a more precise distribution of ultramicropores, where the contribution of ultramicro- ($w < 7$ Å) and micropores ($w < 20$ Å) to the pore volume is considerably higher.

The pore structure characteristics of sol-gel TiC-CDC are compared with the characteristics of CDCs synthesized from commercial (com) TiC and Mo_2C using the chlorination method at 950 °C and 900 °C, respectively (com TiC-CDC and Mo_2C-CDC, respectively) (Table 2). For sol-gel TiC-CDC, a S_{DFT} value of 1560 m^2 g^{-1} and a V_{DFT} value of 2.40 cm^3 g^{-1} is obtained, where ultramicropores make up 5% and micropores (including ultramicropores) make up 22% of the total pore volume for pores with w ranging from 4 Å to 500 Å. Com TiC-CDC and Mo_2C-CDC exhibit micro- and mesopores and S_{DFT} values in similar range (1540 m^2 g^{-1} and 1290 m^2 g^{-1}, respectively). However, the V_{DFT} values of com TiC-CDC and Mo_2C-CDC are considerably lower at 0.68 cm^3 g^{-1} and 1.42 cm^3 g^{-1}, respectively [13,14]. Therefore, although all the investigated CDCs exhibit pores in the same pore width range, and have similar S_{DFT} values, the main difference between the previously studied CDCs and the sol-gel TiC-CDC studied here is the volume of mesopores. Namely, sol-gel TiC-CDC exhibits the largest volume of mesopores of 1.88 cm^3 g^{-1} from pores with $w > 20$ Å, i.e. ~78% out of pores with $w <$ 500 Å.

Table 3 compares the main structural parameters obtained from Raman spectra and WAXS analysis of sol-gel TiC-CDC relative to those of CDCs synthesized by the chlorination method from commercial TiC and Mo_2C at 950 °C and 900 °C, respectively (com TiC-CDC and Mo_2C-CDC). The average stacking size of graphene-like layers, L_c, is much larger for sol-gel TiC-CDC (12.5 Å) compared to com TiC-CDC (5.6 Å) and Mo_2C-CDC (7.7 Å). In contrast, the average graphene-like platelet size, L_a, is in a similar range for all three CDCs (Table 3); from 45 Å for com TiC-CDC to 63 Å for Mo_2C-CDC and 50 Å for sol-gel TiC-CDC. The comparable level of ordered graphene-like platelet domain sizes for all three CDCs is also supported by the Raman analysis; the parameter $I_{\Sigma D}/I_{\Sigma G}$ (Table 3) also exhibits similar values for all three CDCs. The $I_{\Sigma D}/I_{\Sigma G}$ ratio and $FWHM_{DA}$ have been shown to correlate with the structural ordering, i.e., level of graphitization, in carbon materials, where both a lower $I_{\Sigma D}/I_{\Sigma G}$ ratio and a lower $FWHM_{DA}$ are characteristic of a larger coherent graphene-like platelet domain size [40]. Therefore, the main difference between the carbons derived from Mo_2C, sol-gel TiC, and com TiC is the stacking of graphenic layers. The sol-gel TiC-CDC has on average 2.76 graphenic layers per stack, while com TiC-CDC and Mo_2C-CDC have on

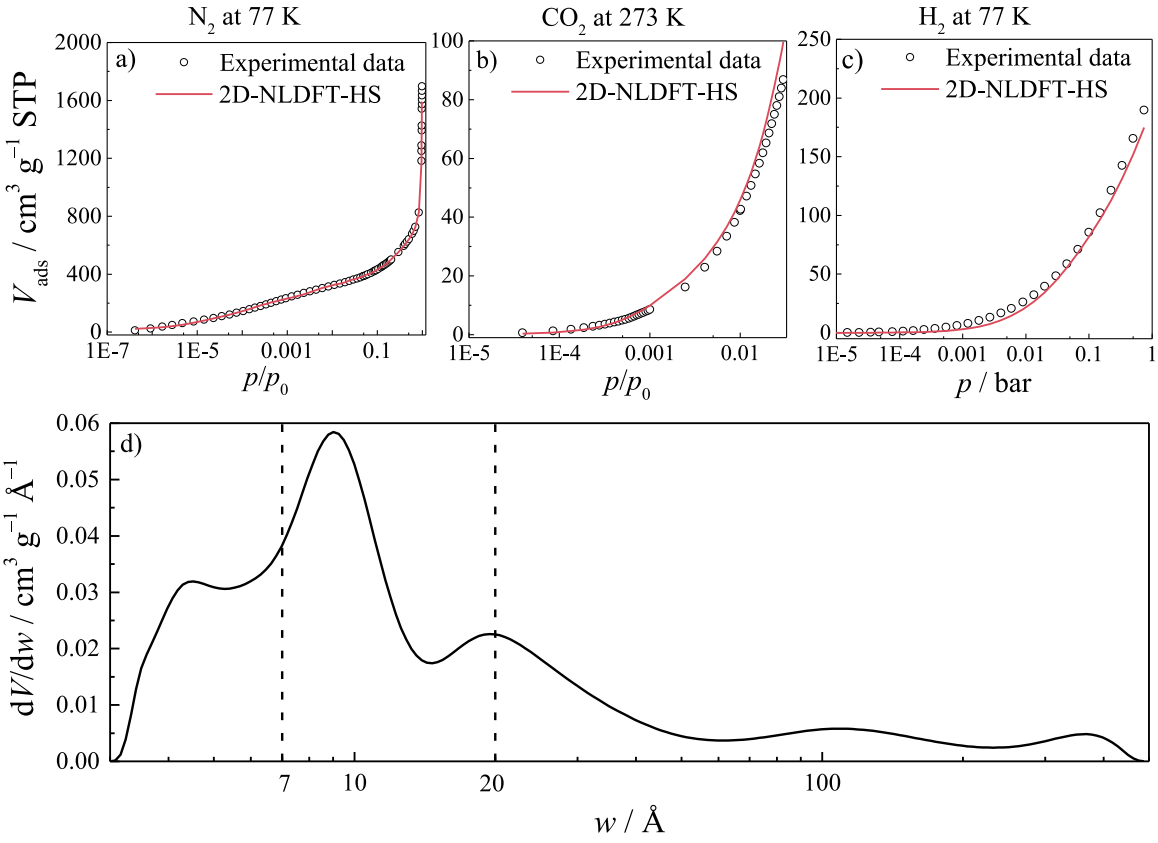

Fig. 3. a) N_2, b) CO_2, and c) H_2 adsorption isotherms fitted globally with the 2D-NLDFT-HS model using the SAIEUS software and d) the calculated pore size distribution of sol-gel TiC-CDC. Vertical dashed lines denote the upper limits of ultramicro- and micropore regions, respectively. (A colour version of this figure can be viewed online.)

Table 2
Pore structure characteristics obtained from the global fitting of multiple gas adsorption isotherms data to the 2D-NLDFT-HS model using SAIEUS software.

Adsorbent	S_{DFT} $m^2\ g^{-1}$	V_{DFT} $cm^3\ g^{-1}$	V_{ump} $cm^3\ g^{-1}$	V_{micro} $cm^3\ g^{-1}$	V_{meso} $cm^3\ g^{-1}$	Ref
Sol-gel TiC-CDC	1560	2.40	0.11	0.52	1.88	This work
Com TiC-CDC	1540	0.68	0.23	0.60	0.08	[14]
Mo_2C-CDC	1290	1.42	0.07	0.33	1.09	[13]

average ≤ 1 layer per stack, meaning that on average, the graphene-like layers are not stacked and do not form ordered domains with each other. In addition, the average interlayer spacing between graphenic layers, a_3, of sol-gel TiC-CDC is lower than in com TiC-CDC and Mo_2C-CDC, indicating greater graphenic interlayer order in sol-gel TiC-CDC.

By comparing the parameters from Raman spectra ($I_{\Sigma D}/I_{\Sigma G}$ and $FWHM_{DA}$) to previously reported parameters from 32 different CDC materials (Fig. 4 from Ref. [40]), it is concluded that based on $FWHM_{DA}$ values, the sol-gel TiC-CDC belongs to the most well-ordered CDC materials, thus containing less defects than com TiC-CDC and Mo_2C-CDC. The sol-gel TiC-CDC stands out with a high ratio of mesopores, relatively high stacking of graphene-like layers for a CDC material, and a relatively well-ordered surface structure compared to the CDCs previously studied with the QENS method. Thus, sol-gel TiC-CDC is a suitable model material with which to investigate the different modes of self-diffusion of H_2 adsorbed in pores with w in the range from 4 Å to 500 Å since it exhibits both very well-ordered regions which should strongly confine the adsorbed H_2 and also mesopores which should promote less restricted self-diffusion of H_2.

Table 3
Main parameters obtained from the deconvolution of Raman spectra and fitting of WAXS patterns.

Material	$I_{\Sigma D}/I_{\Sigma G}$	$FWHM_{DA}$ / cm^{-1}	L_a / Å	L_c / Å	a_3 / Å	$\langle N \rangle$	Ref
Sol-gel TiC-CDC	1.59 ± 0.02	67.4 ± 0.2	50 ± 15	12.5 ± 2.3	3.4 ± 0.2	2.76 ± 0.55	This work
Com TiC-CDC	1.46 ± 0.05	101.2 ± 0.9	45 ± 14	5.6 ± 1.0	3.8 ± 0.2	0.95 ± 0.19	This work, [62]
Mo_2C-CDC	1.25 ± 0.04	81.8 ± 0.7	63 ± 19	7.7 ± 1.4	3.5 ± 0.2	0.79 ± 0.16	[40]

$I_{\Sigma D}/I_{\Sigma G}$ – integrated intensity ratio of D- and G-bands (Eq. (1)) from Raman spectra.
$FWHM_{DA}$ – Full width at half maximum of the deconvoluted D^A band of Raman spectra (Fig. S2).
L_a – average graphene-like platelet size from WAXS.
L_c – average stacking size from WAXS.
a_3 – average interlayer spacing from WAXS.
$\langle N \rangle$ – average number of graphene-like layers per stack from WAXS.

3.2. Self-diffusion of H_2 adsorbed in sol-gel TiC-CDC

To determine the self-diffusion of H_2 adsorbed in sol-gel TiC-CDC, quasi-elastic broadening components are deconvolved from the total neutron scattering spectra, $S(Q,E)$, collected using the MARI and IRIS spectrometers by fitting Eq. (2).

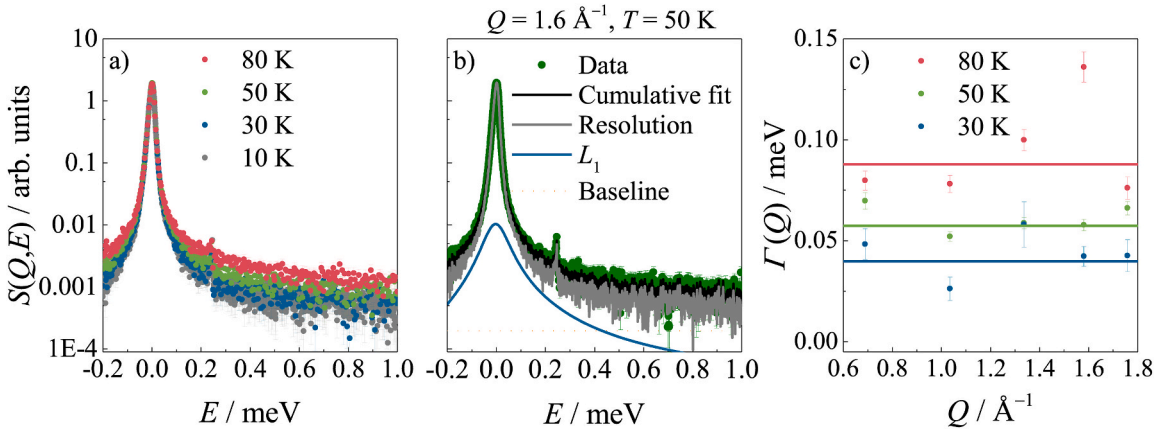

Fig. 4. a) The $S(Q,E)$ measured on IRIS (resolution function at 10 K is just below the $S(Q,E)$ values at 30 K), b) an example of the $S(Q,E)$ at 50 K and at 1.6 Å^{-1} fitted with Eq. 2. and c) the resulting linewidths, $\Gamma(Q)$, of the quasi-elastic broadening for $n_{H2} = 1.7$ mmol g^{-1} as a function of T, where the solid lines denote the $\Gamma(Q)$ values obtained from summed Q values (panel a). (A colour version of this figure can be viewed online.)

3.2.1. *Self-diffusion of strongly confined H_2*

At $n_{H2} \geq 1.7$ mmol g^{-1} and $T \geq 30$ K, the neutron scattering spectra of H_2 adsorbed in sol-gel TiC-CDC exhibit a weak quasi-elastic signal relative to the instrument resolution function; the latter being measured at 10 K (Fig. 4a). This quasi-elastic broadening indicates that the increase in temperature provides enough additional kinetic energy to the adsorbed H_2 for self-diffusion processes to be noted at a T as low as 30 K. Observation of the self-diffusion of adsorbed H_2 at 30 K is possible due to the experimental time window accessed by the IRIS spectrometer (~5 ps – 150 ps) (Table 1).

The Q-independent linewidth (Fig. 4c) of the quasi-elastic broadenings measured at $n_{H2} = 1.7$ mmol g^{-1}, component L_1, is indicative of localized or constrained self-motion, and, as suggested by Fig. 6.14 in Ref. [43], the H_2 adsorbed in ultramicropores is assumed to self-diffuse rotationally (SI section 6 Fig. S10). The presence of localized rotational self-diffusion of H_2 in narrow ultramicropores could be caused by only one energy minimum at these adsorption sites which restrict translational motions of the adsorbed H_2 molecules [15]. The PSD analysis showed that the volume ultramicropores make up ~5 % out of pores with w in the range of 4 Å to 500 Å (section 3.1).

The residence times between two rotational jumps decrease from ~9 ps to ~3 ps (considering that 1 meV = 1.52 10^{12} rad s^{-1} from Fig. 4, see SI Figure S8) with the increase in T from 30 K to 80 K. This indicates a temperature-induced increase in the rotational self-diffusion of adsorbed H_2. For comparison, the characteristic rotational self-diffusion time of H_2 adsorbed in mesoporous carbon [45] and exfoliated graphite [45] are in the range of ~0.1 ps - 2 ps in the T range from 22 K to 80 K. Since the residency times between rotational jumps of H_2 adsorbed in the carbon studied here are longer, the ultramicropores of sol-gel TiC-CDC can more effectively confine adsorbed H_2.

Although the self-diffusion of H_2 adsorbed in CDCs has been previously investigated [13,14,16], this is the first time that slow rotational self-diffusion of H_2 adsorbed in CDCs has been observed. This is possible due to the shifted temporal range, from 5 ps to 150 ps (Table 1), afforded by the IRIS spectrometer (i.e., slower dynamics being probed), compared to that of the NEAT and FOCUS instruments used in previous studies [13,14]. Therefore, it is likely that if the self-diffusion of H_2 adsorbed in Mo_2C-CDCs were investigated using an instrument with the same energy resolution as IRIS, rotational self-diffusion might have also been observed.

Contescu et al. observed an even more restricted translational self-diffusion of H_2 adsorbed in polyfurfuryl alcohol-derived activated carbon (PFAC) and ultramicroporous carbon (UMC) in Ref. [16]. This could be related to the level of surface coverage and the number of available adsorption sites. In Ref. [16] the excess H_2 was outgassed from the sample container, meaning that only very strongly adsorbed H_2 is left in the sample and, thus, the presumably lower surface coverage yields more available adsorption sites compared to the H_2 adsorbed in sol-gel TiC-CDC, investigated in this work. Therefore, the partial surface coverage and availability of free neighboring adsorption sites allows H_2 adsorbed in PFAC and UMC to perform translational jumps from one adsorption site with higher likelyhood. Whereas in sol-gel TiC-CDC, at higher H_2 surface coverage the high energy adsorption sites are fully occupied, lowering the likelyhood for translational jumps and promoting and/or making it possible to detect only the predominant rotational self-diffusion.

3.2.2. *Self-diffusion of mobile H_2*

Translational jump-diffusion models can be used to describe the dependency of $\Gamma(Q)$ upon Q, yielding information about the self-diffusion of adsorbed H_2. The translational jump-diffusion model used in this work, the Hall-Ross model (Eq. (3)), assumes that the jump lengths follow a Gaussian distribution (Eq. (4)) and describes jump diffusion in a restricted volume, e.g., in narrow pores [61].

$$\Gamma(Q) = \frac{\hbar}{\tau}\left(1 - \exp\left(-Q^2 \tau D\right)\right) \tag{3}$$

$$\rho(l) = \frac{2l^2}{l_0^2\sqrt{2\pi}} \exp\left(-\frac{l^2}{2l_0^2}\right) \tag{4}$$

where ħ is the reduced Planck constant, τ is the residency time, D is the translational diffusion coefficient, $\rho(l)$ is the distribution of jump lengths, $\langle l \rangle$ is the mean jump length, and l_0 is the distribution mode value, where $\langle l^2 \rangle = 3l_0^2$ (where $\langle l^2 \rangle$ is the mean square jump length) and $\langle l \rangle = \sqrt{6\tau D}$.

From the data obtained on the MARI spectrometer, two linewidths per loading within the experimental time window afforded by the instrument could be resolved. At $n_{H2} \geq 10$ mmol g^{-1} and $T \geq 50$ K, when H_2 is adsorbed in both micro- and mesopores, the self-diffusion of H_2 takes place on multiple timescales, expressed as distinct quasi-elastic broadenings. Information about each QENS signal is obtained by deconvolution with multiple Lorentzian distributions (Fig. 5a and b), as has been shown in Refs. [13,24–26,62]. The narrower of the two Lorentzian distributions (L_2) is determined from IRIS $S(Q,E)$ at $n_{H2} = 10$ mmol g^{-1} and is fixed to resolve the broader Lorentzian distribution more reliably.

The Q-dependence of $\Gamma(Q)$ observed at $n_{H2} \geq 10$ mmol g^{-1} and $T \geq 50$ K (Fig. 5c,d and Fig. S14 in SI) indicates that the H_2 adsorbed in micro- and mesopores is self-diffusing translationally. The $\Gamma(Q)$ of the L_2, $L_{3.10}$, and $L_{3.31}$ components vs Q are fitted using the Hall-Ross jump-

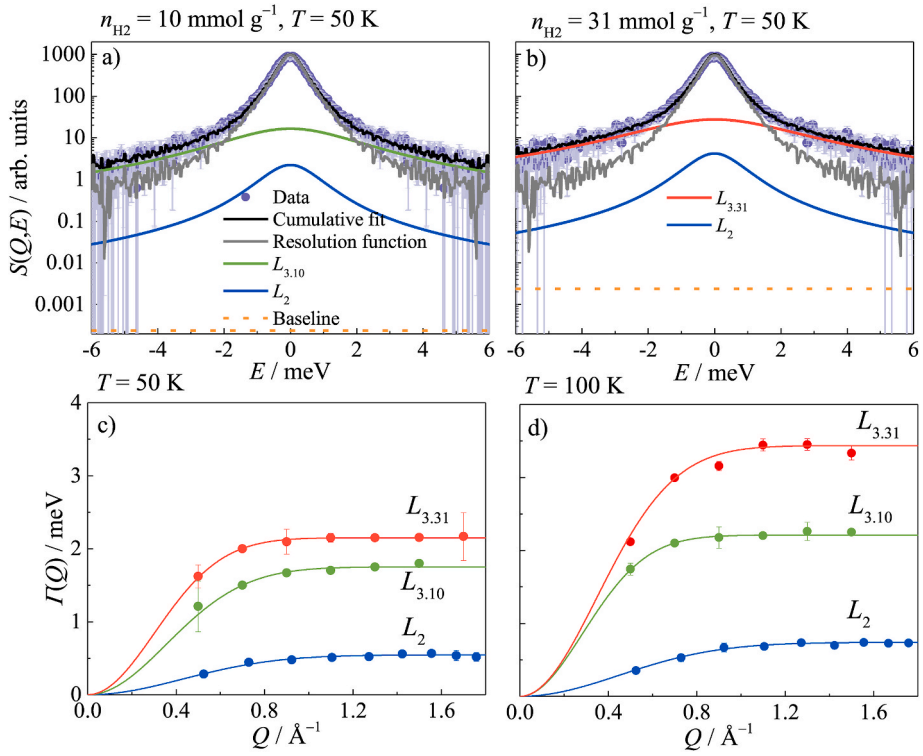

Fig. 5. The $S(Q,E)$ at $Q = 1.3$ Å^{-1} and 50 K collected on MARI at a) at $n_{H2} = 10$ mmol g^{-1} and b) $n_{H2} = 31$ mmol g^{-1}, where L_2, $L_{3.10}$ and $L_{3.31}$ denote the quasi-elastic components obtained from fitting Eq. (2) to the data. The $\Gamma(Q)$ of the quasi-elastic broadening components L_2, $L_{3.10}$, and $L_{3.31}$ at c) 50 K and d) 100 K fitted with the Hall-Ross jump-diffusion model (solid lines from Eq. (3)). (A colour version of this figure can be viewed online.)

diffusion model (Eq. (3)), which presumes that the self-diffusion is taking place in a restricted volume, i.e., H_2 is adsorbed in pores with a clear confining volume and is further restricted by neighboring H_2 molecules. The three different H_2 translational self-diffusion mobilities are attributed to the H_2 transport in different adsorption layers, where H_2 is adsorbed in:

1. layers closer to the pore wall, e.g., in the monolayer denoted with L_2;
2. layers more in the middle region of the pore at $n_{H2} = 10$ mmol g^{-1}, e. g., subsequent H_2 layers on top of the monolayer, denoted with $L_{3.10}$, where subscript 10 denotes the total amount of H_2 per 1 g of sol-gel TiC-CDC in the closed sample cell in mmol g^{-1};
3. layers more in the middle region of the pore at $n_{H2} = 31$ mmol g^{-1}, e. g., subsequent H_2 layers on top of the monolayer, denoted with $L_{3.31}$, where subscript 31 denotes the total amount of H_2 per 1 g of sol-gel TiC-CDC in the closed sample cell in mmol g^{-1}.

At $n_{H2} \geq 10$ mmol g^{-1}, when H_2 is adsorbed also in larger pores, i.e., in micro- and mesopores, ~130% and ~290% of the surface of sol-gel TiC-CDC is covered with H_2 at 20 K, respectively. As a result, while some of the H_2 is adsorbed on top of the H_2 monolayer in subsequent H_2 layers the majority congregates in the middle region of the pore. The H_2 components adsorbed in subsequent layers ($L_{3.10}$ and $L_{3.31}$) have more freedom to self-diffuse and the confining effect of ultramicropores becomes less evident when compared to H_2 self-diffusivity at $n_{H2} = 1.7$ mmol g^{-1}. This is indicated by the difference in magnitude of HWHM values of the quasi-elastic broadenings at $n_{H2} = 1.7$ mmol g^{-1} (HWHM <0.15 meV, Fig. 4b) compared to those at $n_{H2} \geq 10$ mmol g^{-1} (HWHM in the range of 0.3 meV–3.5 meV, Fig. 5c and d). With the increase in temperature from 50 K to 100 K, the translational self-diffusion coefficients, D, of all H_2 components increase and the residency times between jumps, τ, of all H_2 components decrease (Table 4). As the temperature increases, H_2 desorbs from the pores, i.e., the surface coverage and the steric hindrance from neighboring adsorbed H_2 decreases. Therefore, as T increases, the adjacent H_2 molecules have more room and kinetic energy to self-diffuse.

Table 4
Translational jump-diffusion parameters of H_2 adsorbed in sol-gel TiC-CDC.

Parameter	H_2 component	n_{H2} / mmol g^{-1}	T = 50 K	T = 80 K	T = 100 K
τ 10^{-12} [a] s	L_2	≥10	1.21 ± 0.02	0.98 ± 0.02	0.89 ± 0.01
	$L_{3.10}$	10	0.38 ± 0.01	0.30 ± 0.01	0.30 ± 0.01
	$L_{3.31}$	31	0.31 ± 0.01	0.21 ± 0.01	0.19 ± 0.01
D 10^{-8} [b] m^2 s^{-1}	L_2	≥10	2.3 ± 0.1	2.6 ± 0.2	2.8 ± 0.2
	$L_{3.10}$	10	10.5 ± 0.3	15.5 ± 0.2	20.6 ± 0.5
	$L_{3.31}$	31	17.9 ± 0.2	19.9 ± 1.1	21.6 ± 1.1

[a] residency time between jumps.
[b] translational self-diffusion coefficient.

An Arrhenius-type equation can be used to describe the temperature dependence of the diffusion coefficients of H_2 adsorbed in porous carbons (Eq. 5) [13,43]. By applying this relation, the activation energy of the diffusion process, E_a, and the extrapolated diffusion coefficient at infinite temperature, D_0, can be calculated from the slope and intercept of the graph, respectively.

$$D = D_0 \exp\left(-\frac{E_a}{RT}\right) \quad (5)$$

where R is the universal gas constant and T is the temperature.

Since the logarithmic values of D-s are linear with respect to the inverse value of T, an Arrhenius relation can be applied to calculate the activation energies, E_a, and maximal diffusion coefficients, D_0 (Eq. (5),

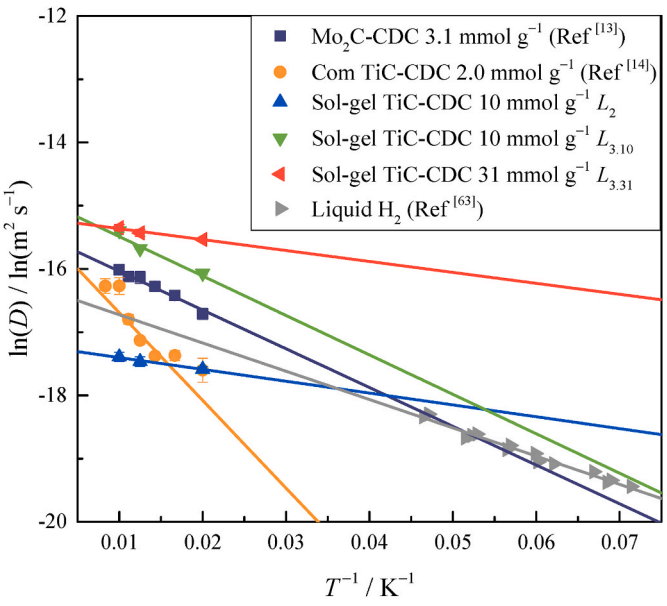

Fig. 6. Arrhenius type plot showing diffusion coefficients of H_2 adsorbed in CDCs from previous work [13,14] and from this work at various amounts of total H_2 in the sample cell per adsorbent mass, n_{H2} (noted in the figure). The diffusion coefficient of bulk liquid H_2 from Ref. [63] is shown for comparison alongside Arrhenius type description of the data (Eq. (5), solid lines). (A colour version of this figure can be viewed online.)

Fig. 6) of H_2 translational jumps. The corresponding values for the self-diffusion of H_2 adsorbed in Mo_2C-CDC and com TiC-CDC are reported in Table 5 for comparison.

The differences between E_a and D_0 values for the self-diffusion of H_2 adsorbed in Mo_2C-CDC and com TiC-CDC compared to that of sol-gel TiC-CDC do not arise only from the differences in the graphenic and porous structure of the adsorbent, but also from the differences in the deconvolution procedure applied to the $S(Q,E)$. Namely, the self-diffusion of H_2 adsorbed in Mo_2C-CDC and com TiC-CDC was analyzed as self-diffusion on one timescale (i.e., fitted with one Lorentzian function to account for one type of H_2 motion) [13,14]. The self-diffusion of H_2 adsorbed in sol-gel TiC-CDC, on the other hand, is analyzed as self-diffusion across multiple separable timescales (i.e., fitted with multiple Lorentzian functions) to differentiate between the self-diffusion of H_2 adsorbed both as a monolayer and as subsequent layers. Such multi-component analysis across a wide temporal range is possible by combining data from different measurement setups and instruments.

The proposed mechanism for the diffusion of adsorbed H_2 between different adsorption sites in monolayer and subsequent layers can be seen in Fig. 7. The relatively low E_a value of L_2 indicates that H_2 adsorbed in the monolayer of sol-gel TiC-CDC can jump between the strong adsorption centers with almost no restriction. It has been shown that the differences in binding energies of H_2 adsorbed in strong binding sites can be small and, as such, there could be many equally preferred adsorption sites [64,65]. The monolayer H_2 is strongly confined to the pore wall and is not able to diffuse toward the middle region of the pore as indicated by the low D_0 value. The strong confinement of the H_2 molecules adsorbed as a monolayer can be explained by the type of interactions they experience. Namely, H_2 molecules adsorbed in monolayer and in pores with $w < 10$ Å are strongly influenced by the adjacent pore walls [15] and the H_2 molecule interacts with neighboring and subsequent H_2 molecules, therefore experiencing confinement from every direction [66]. The presence of strongly confined H_2 monolayer has also been suggested in the mesopores of the mesoporous silica KIT-6, where it was reported that the bulk-liquid and bulk-solid densities of H_2 could be exceeded by a factor of almost 3 [67]. The formation of such a high-density adsorbed H_2 monolayers was proposed to be possible only on smooth adsorbent surfaces and at temperatures close to that of liquid H_2 (i.e., near 20 K) [67].

Table 5
H_2 amounts and results from Arrhenius type equation.

Adsorbent	n_{H2} / mmol g^{-1}	E_a / kJ mol^{-1}	D_0 10^{-7} / m^2 s^{-1}	Reference
Mo_2C-CDC	3.1	0.70 ± 0.14	1.49 ± 0.38	[13]
Com TiC-CDC	2.0	1.18 ± 0.18	1.11 ± 0.33	[14]
Sol-gel TiC-CDC L_2	10	0.17 ± 0.01	0.34 ± 0.07	This work
Sol-gel TiC-CDC $L_{3.10}$	10	0.50 ± 0.12	3.44 ± 0.72	This work
Sol-gel TiC-CDC $L_{3.31}$	31	0.14 ± 0.02	2.53 ± 0.11	This work

The H_2 component adsorbed in subsequent layers at $n_{H2} = 10$ mmol g^{-1} ($L_{3.10}$) can be envisaged as the H_2 diffusing from strongly bound monolayer to subsequent layers and therefore has a slightly higher E_a value (Fig. 7, Table 5). When this slightly higher activation barrier is exceeded, this H_2 component is mobile as indicated by the relatively higher D_0 value. The H_2 adsorbed in subsequent layers does not experience as strong interaction with the pore wall as in the monolayer because they are further separated. This means that the confinement arises mainly from steric hindrance and therefore the H_2 is more mobile than in monolayer [66]. The H_2 component adsorbed in subsequent layers at $n_{H2} = 31$ mmol g^{-1}, $L_{3.31}$, is able to self-diffuse between the weaker adsorption sites and within the adsorbed H_2 regions with virtually no restriction, as indicated by the low E_a and high D_0 value. This can be explained by the differences in densities of different regions - the density of H_2 in subsequent layers is lower than in monolayer, i.e., fewer intermolecular interactions are involved [68].

Considering jump length distributions calculated with the Hall-Ross model, approximately 50% of the jumps of the self-diffusive H_2 adsorbed in monolayer (L_2) are in the range 3 Å to 7 Å (Fig. 8a). Theoretically, the possible jumps of H_2 adsorbed in high energy adsorption sites on an ideal graphene surface have been calculated to be in the range of ~3 Å to ~5 Å along the plane depending on the specific position of the H_2 molecule [65,66]. The surface of sol-gel TiC-CDC, however, is not ideal and has defects (section 3.1) that provide additional high-energy adsorption sites. Therefore, ~50% of the jumps of H_2 adsorbed in the monolayer of sol-gel TiC-CDC could be between the strong neighboring adsorption sites which are provided by the ultramicropores. In addition, the H_2 adsorbed in high-energy adsorption sites could perform longer jumps during a jump event as the nearest adsorption positions could already be fully occupied by adsorbed H_2 molecules [64]. Therefore, even longer jumps between strong binding sites are possible, as indicated in Fig. 8a by the jump length distributions going to the maximal value of ~15 Å.

The jump length distributions of H_2 adsorbed in subsequent layers at $n_{H2} = 10$ mmol g^{-1} and $n_{H2} = 31$ mmol g^{-1} ($L_{3.10}$, and $L_{3.31}$, respectively) are more spread out, extending to the maximal value of ~20 Å – 25 Å (Fig. 8b and c). This confirms that the H_2 fractions are no longer jumping mainly between the high-energy adsorption sites but could be diffusing from the monolayer to the middle region of the pore and self-diffuse without significant restriction within the subsequent layers. The mean jump lengths, 6.6 ± 1.7 Å, of H_2 adsorbed more towards the middle region of the pore at 50 K and at $n_{H2} = 31$ mmol g^{-1} have a large uncertainty, meaning that it is indiscernible over temperatures of 80 K–100 K, where the mean jump lengths are ~5 Å (Table S9 in SI in section 6). This suggests that when H_2 is adsorbed more in the middle region of the pore, the microporous and graphenic structure of the carbon adsorbent does not affect the confinement of more mobile H_2 molecules that strongly anymore. As a result, the H_2 is relatively mobile within the phase.

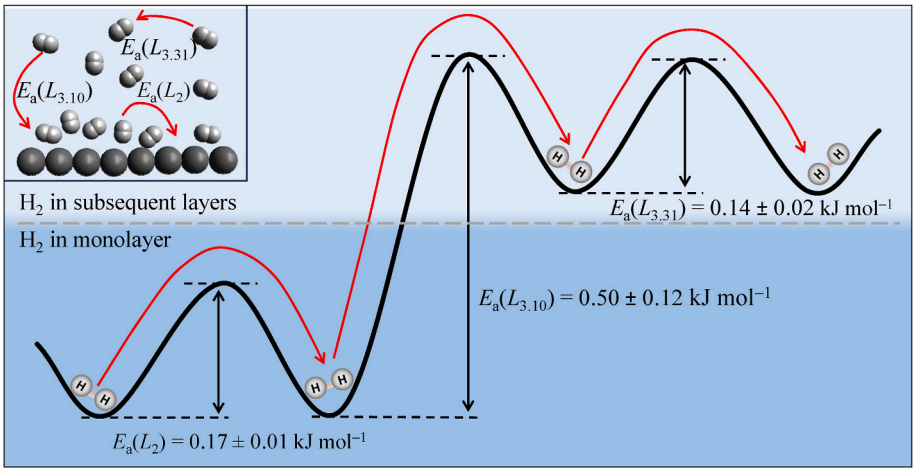

Fig. 7. The proposed mechanism for the diffusion of adsorbed H_2 between different adsorption sites in monolayer and subsequent layers and the schematic representations of the H_2 translational jumps corresponding to different averaged E_a values are shown in the inset. (A colour version of this figure can be viewed online.)

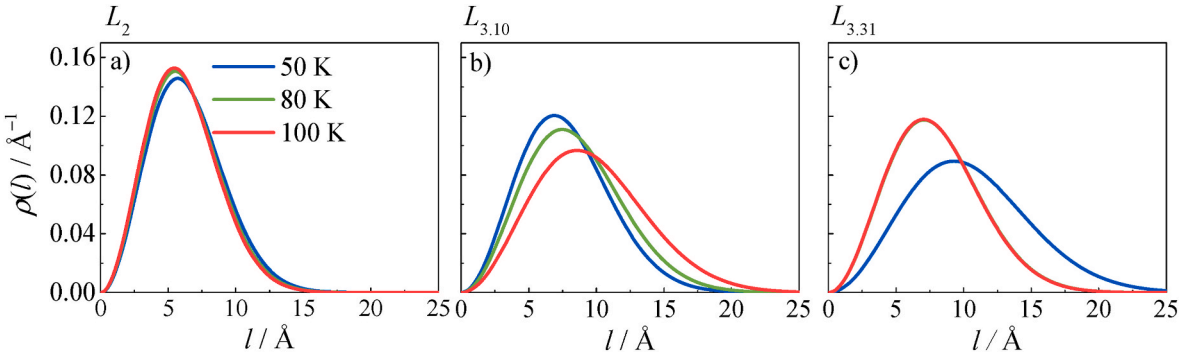

Fig. 8. Jump length distributions calculated with the Hall-Ross model describing translational jump diffusion in restricted volume (Eq. (4)) for adsorbed H_2 components a) L_2, b) $L_{3.10}$, and c) $L_{3.31}$. (A colour version of this figure can be viewed online.)

3.3. Comparison with other CDCs

The self-diffusion of H_2 adsorbed in Mo_2C-CDC [13,14] and in com TiC-CDC [14] at $n_{H2} = 3.1$ mmol g^{-1} and $n_{H2} = 2.0$ mmol g^{-1}, respectively, follow a translational jump-like diffusion mode like in sol-gel TiC-CDC. This is evident from the similar shape of the HWHM vs Q as well as the D values, which follow an Arrhenius-type relation (Fig. 6). Therefore, similar self-diffusional processes, i.e. where the self-diffusion process has an activation barrier and where the adsorbed H_2 molecules are restricted by the pore walls of the adsorbents and/or adjacent H_2 molecules, are taking place in the investigated CDCs.

The differences between the self-diffusion processes of H_2 adsorbed in different CDCs become evident when comparing τ values extracted from CDCs under common experimental conditions. Here, τ is effectively dependent on the height of the plateau observed from $\Gamma(Q)$ vs Q and extracted when this response is fitted with the Hall-Ross [61], Sing-wi-Sjölander [69] or Chudley-Elliot model [70]. The τ values of H_2 adsorbed in the monolayer in Mo_2C-CDCs (from ~2.8 ps to ~1.0 ps at 50 K–100 K, respectively) (supplementary information of Ref [13]) are longer than in sol-gel TiC-CDC (from ~1.2 ps to ~0.9 ps at 50 K–100 K, respectively) (Table 4). This indicates that Mo_2C-CDC can confine the H_2 adsorbed in monolayer to a larger extent than sol-gel TiC-CDC (L_2). This could be related to a higher degree of graphenization (i.e., stacking of graphene-like layers and less defects) and larger volume of mesopores in sol-gel TiC-CDC compared to the rest of the CDCs (section 3.1). The interlayer distance in graphenic non-graphitic carbon materials (3.3 Å – 3.7 Å) is too narrow for H_2 adsorption and, therefore, if the graphene-like layers are ordered in stacks of more than one layer (2.76 graphene-like layers for sol-gel TiC-CDC), important sites for H_2 adsorption are lost. In addition, the larger volume of mesopores in sol-gel TiC-CDC compared to Mo_2C-CDC promotes faster self-diffusion of H_2 adsorbed in monolayer (L_2) and, therefore, shorter τ values of adsorbed H_2 compared to Mo_2C-CDC.

The τ values of translationally self-diffusive H_2 adsorbed in subsequent layers of sol-gel TiC-CDC (i.e., $L_{3.10}$ and $L_{3.31}$) are the shortest at $n_{H2} = 31$ mmol g^{-1} (~0.19 ps), indicating the highest self-diffusivity. Similar τ values (0.18 ± 0.01 ps) were observed for H_2 adsorbed in Mo_2C-CDCs studied with the NEAT instrument set up for resolution of 0.1 meV [13] despite the fact that NEAT has a temporal range shifted to observe slower motions compared to MARI. Moreover, sol-gel TiC-CDC (investigated with instrument MARI) has a larger volume of mesopores, larger stacking of graphenic sheets and smaller interlayer spacing compared to Mo_2C-CDC (Table 3), which should even further promote faster self-diffusion and smaller τ values. However, faster self-diffusion of H_2 adsorbed in sol-gel TiC-CDC is not seen. Therefore, when H_2 is adsorbed in CDCs, the τ values of ~0.19 ps could be the minimal time between jumps in translational jump-like diffusion mode. Thus, based on these results, when n_{H2} values are high and H_2 is already adsorbed in subsequent layers and in mesopores, then the influence of the graphenic and microporous structure of the CDCs on the confinement of adsorbed H_2 is limited.

4. Conclusion

The self-diffusional dynamics of H_2 adsorbed in sol-gel TiC-CDC adsorbent is investigated with *in situ* the quasi-elastic neutron scattering

(QENS) method over a wide temporal range. The experiments are carried out at temperatures in the range from 10 K to 100 K and at different H_2 loading conditions, ensuring different levels of surface coverage.

In-depth structural analysis of sol-gel TiC-CDC revealed that the main difference between the carbons derived from Mo_2C, sol-gel and commercial TiC is the stacking of graphenic layers. While TiC-CDC and Mo_2C-CDCs synthesized from commercial carbides have on average up to one graphene-like layer per stack, the sol-gel TiC-CDC has on avergae 2.76 graphene-like layers per stack and the interlayer spacing is also smaller between graphene-like layers in graphenic stacks.

When H_2 is adsorbed mostly in ultramicropores, i.e., the high energy adsorption sites present in sol-gel TiC-CDC, a fraction of the H_2 is able to self-diffuse already at 30 K and the self-diffusion mechanism of the adsorbed H_2 is rotational. This is the first time when the very slow rotational self-diffusion of H_2 adsorbed in CDCs is observed. When H_2 is adsorbed in micro- and mesopores of sol-gel TiC-CDC, the self-diffusion of the adsorbed H_2 is translational and takes place over multiple timescales. The components of H_2 self-diffusing in multiple timescales is interpreted as the separable self-diffusion of H_2 adsorbed closer to the pore wall, i.e., in the monolayer, and H_2 adsorbed farther away from the pore wall and in the middle region of the pore, i.e., in subsequent layers. Such distinction between components of adsorbed H_2 across a wide temporal range is possible by combining QENS data from different measurement setups and instruments.

The self-diffusion of H_2 adsorbed in the monolayer in Mo_2C-CDC is considerably more restricted than in sol-gel TiC-CDC. This is related to a higher degree of graphenization and larger volume of mesopores in sol-gel TiC-CDC compared to the rest of the CDCs. The shortest residency time between jumps is ~0.19 ps for H_2 adsorbed in subsequent layers in sol-gel TiC-CDC is very similar to the residency time (~0.18 ps) of H_2 adsorbed in Mo_2C-CDCs obtained from measurement data on the NEAT instrument at similar experimental conditions. However, the experiment on MARI spectrometer was set up to access considerably faster H_2 dynamics than NEAT. This suggests that under high H_2 loadings and in case of H_2 adsorption in subsequent layers and in mesopores the graphenic and microporous structure of the CDCs does not anymore have considerbale effect on the confinement of adsorbed H_2.

In this work we present the simultaneous determination and disentanglement of H_2 motions across different timescales. This methodology allowed to analyze the dynamics of H_2 adsorbed in high density phase at conditions which are close to the ones used in technical applications. The presented methodology and results yield vital insight into H_2 adsorbent interaction for cryo-adsorptive system development.

CRediT authorship contribution statement

Miriam Koppel: Conceptualization, Formal analysis, Investigation, Methodology, Visualization, Writing – original draft. **Rasmus Palm:** Conceptualization, Formal analysis, Funding acquisition, Methodology, Project administration, Supervision, Writing – original draft. **Riinu Härmas:** Conceptualization, Formal analysis, Supervision, Writing – original draft. **Mark Telling:** Conceptualization, Investigation, Methodology, Writing – review & editing. **Manh Duc Le:** Writing – review & editing. **Tatiana Guidi:** Writing – review & editing. **Kenneth Tuul:** Writing – review & editing. **Maarja Paalo:** Investigation, Resources, Writing – review & editing. **Laura Kalder:** Formal analysis, Visualization, Writing – review & editing. **Jacek Jagiello:** Formal analysis, Writing – review & editing. **Tavo Romann:** Investigation, Writing – review & editing. **Jaan Aruväli:** Investigation, Writing – review & editing. **Martin Månsson:** Writing – review & editing. **Enn Lust:** Funding acquisition, Project administration, Supervision, Writing – review & editing.

Declaration of competing interest

The authors declare the following financial interests/personal relationships which may be considered as potential competing interests: Enn Lust reports financial support was provided by Archimedes Foundation. Enn Lust reports financial support was provided by Estonian Ministry of Education and Research. Rasmus Palm reports financial support was provided by Estonian Research Council. Enn Lust reports was provided by Estonian Research Council. Rasmus Palm reports financial support was provided by Ragnar Holm Foundation. Martin Mansson reports financial support was provided by Swedish Foundation for Strategic Research. Martin Mansson reports financial support was provided by Carl Tryggers Foundation for Scientific Research. If there are other authors, they declare that they have no known competing financial interests or personal relationships that could have appeared to influence the work reported in this paper.

Acknowledgements

The authors wish to express their gratitude for the support offered by the staff of ISIS pulsed neutron and muon source, and thank the Science and Technology Facilities Council for beamtime allocation RB2010339 and RB2010603. This research was supported by the EU through the European Regional Development Fund (Centers of Excellence, TK141 “Advanced materials and high-technology devices for sustainable energetics, sensorics and nanoelectronics”), by the Estonian Ministry of Education and Research through funding from SLTKT16432T “Estonian participation in designing, construction and application of the ESS 1.09.2015–31.08.2023)", as well as by the Estonian Research Council through Grants PUTJD957 and PRG676. KTH acknowledges funding from the Ragnar Holm Foundation, the Swedish Research Council (VR, Dnr. 2021-06157 and Dnr. 2022-03936), the Swedish Foundation for Strategic Research (SSF, SwedNess), and the Carl Tryggers Foundation for Scientific Research (CTS-18:272 CTS-22:2374).

Appendix A. Supplementary data

Supplementary data to this article can be found online at https://doi.org/10.1016/j.carbon.2024.118799.

References

[1] E. Masika, R. Mokaya, Hydrogen storage in high surface area carbons with identical surface areas but different pore sizes: direct demonstration of the effects of pore size, J. Phys. Chem. C 116 (49) (2012) 25734–25740, https://doi.org/10.1021/jp3100365.
[2] C.I. Contescu, H. Zhang, R.J. Olsen, E. Mamontov, J.R. Morris, N.C. Gallego, Isotope effect on adsorbed quantum phases: diffusion of H2 and D2 in nanoporous carbon, Phys. Rev. Lett. 110 (23) (2013) 236102, https://doi.org/10.1103/PhysRevLett.110.236102.
[3] R. Jäger, P.E. Kasatkin, E. Härk, E. Lust, Oxygen reduction on molybdenum carbide derived micromesoporous carbon electrode in alkaline solution, Electrochem. Commun. 35 (2013) 97–99, https://doi.org/10.1016/j.elecom.2013.08.001.
[4] V. Dias, M. Pochet, F. Contino, H. Jeanmart, Energy and economic costs of chemical storage, Front. Mech. Eng. 6 (2020).
[5] R.B. Gupta, Hydrogen Fuel: Production, Transport, and Storage, CRC Press, 2008.
[6] G. Petitpas, P. Bénard, L.E. Klebanoff, J. Xiao, S. Aceves, A comparative analysis of the cryo-compression and cryo-adsorption hydrogen storage methods, Int. J. Hydrogen Energy 39 (20) (2014) 10564–10584, https://doi.org/10.1016/j.ijhydene.2014.04.200.
[7] J. Rogacka, L. Firlej, B. Kuchta, Modeling of low temperature adsorption of hydrogen in carbon nanopores, J. Mol. Model. 23 (1) (2017) 20, https://doi.org/10.1007/s00894-016-3202-y.
[8] J.J.M. Beenakker, V.D. Borman, S. Yu Krylov, Molecular transport in subnanometer pores: zero-point energy, reduced dimensionality and quantum sieving, Chem. Phys. Lett. 232 (4) (1995) 379–382, https://doi.org/10.1016/0009-2614(94)01372-3.
[9] N.C. Gallego, L. He, D. Saha, C.I. Contescu, Y.B. Melnichenko, Hydrogen confinement in carbon nanopores: extreme densification at ambient temperature, J. Am. Chem. Soc. 133 (35) (2011) 13794–13797, https://doi.org/10.1021/ja202432x.
[10] V.P. Ting, et al., Direct evidence for solid-like hydrogen in a nanoporous carbon hydrogen storage material at supercritical temperatures, ACS Nano 9 (8) (2015) 8249–8254, https://doi.org/10.1021/acsnano.5b02623.
[11] J. Bahadur, et al., Properties of immobile hydrogen confined in microporous carbon, Carbon 117 (2017) 383–392, https://doi.org/10.1016/j.carbon.2017.03.007.

[12] M. Koppel, et al., In situ observation of pressure modulated reversible structural changes in the graphitic domains of carbide-derived carbons, Carbon 174 (2021) 190–200, https://doi.org/10.1016/j.carbon.2020.12.025.
[13] M. Koppel, et al., Pore wall corrugation effect on the dynamics of adsorbed H2 studied by in situ quasi-elastic neutron scattering: observation of two timescaled diffusion, Carbon 197 (2022) 359–367, https://doi.org/10.1016/j.carbon.2022.06.061.
[14] R. Härmas, et al., Transport properties of H2 confined in carbide-derived carbons with different pore shapes and sizes, Carbon 155 (2019) 122–128, https://doi.org/10.1016/j.carbon.2019.08.041.
[15] M. Konstantakou, A. Gotzias, M. Kainourgiakis, A.K. Stubos, T.A. Steriotis, GCMC Simulations of Gas Adsorption in Carbon Pore Structures, IntechOpen, 2011, https://doi.org/10.5772/15988.
[16] C.I. Contescu, D. Saha, N.C. Gallego, E. Mamontov, A.I. Kolesnikov, V.V. Bhat, Restricted dynamics of molecular hydrogen confined in activated carbon nanopores, Carbon 50 (3) (2012) 1071–1082, https://doi.org/10.1016/j.carbon.2011.10.016.
[17] Y. Gogotsi, R.K. Dash, G. Yushin, T. Yildirim, G. Laudisio, J.E. Fischer, Tailoring of nanoscale porosity in carbide-derived carbons for hydrogen storage, J. Am. Chem. Soc. 127 (46) (2005) 16006–16007.
[18] Y. Gogotsi, et al., Importance of pore size in high-pressure hydrogen storage by porous carbons, Int. J. Hydrogen Energy 34 (15) (2009) 6314–6319, https://doi.org/10.1016/j.ijhydene.2009.05.073.
[19] G. Laudisio, R.K. Dash, J.P. Singer, G. Yushin, Y. Gogotsi, J.E. Fischer, Carbide-derived carbons: a comparative study of porosity based on small-angle scattering and adsorption isotherms, Langmuir 22 (21) (2006) 8945–8950, https://doi.org/10.1021/la060860e.
[20] R.S. Aga, C.L. Fu, M. Krčmar, J.R. Morris, Theoretical investigation of the effect of graphite interlayer spacing on hydrogen absorption, Phys. Rev. B 76 (16) (2007) 165404, https://doi.org/10.1103/PhysRevB.76.165404.
[21] G. Sdanghi, R.L.S. Canevesi, A. Celzard, M. Thommes, V. Fierro, Characterization of Carbon Materials for Hydrogen Storage and Compression," C 6 (3) (2020), https://doi.org/10.3390/c6030046. Art. no. 3.
[22] M. Rzepka, P. Lamp, M.A. de la Casa-Lillo, Physisorption of hydrogen on microporous carbon and carbon nanotubes, J. Phys. Chem. B 102 (52) (1998) 10894–10898, https://doi.org/10.1021/jp9829602.
[23] L. Peng, J. Morris, Prediction of hydrogen adsorption properties in expanded graphite model and in nanoporous carbon, J. Phys. Chem. C 114 (2010) 15522–15529, https://doi.org/10.1021/jp104595m.
[24] Y. Yang, et al., Micro-channel development and hydrogen adsorption properties in templated microporous carbons containing platinum nanoparticles, Carbon 49 (4) (2011) 1305–1317, https://doi.org/10.1016/j.carbon.2010.11.050.
[25] J. DeWall, R.M. Dimeo, P.E. Sokol, Slow diffusion of molecular hydrogen in zeolite 13X, J. Low Temp. Phys. 129 (2002) 171–184, https://doi.org/10.1023/A:1020896123362.
[26] H. Fu, F. Trouw, P.E. Sokol, A quasi-elastic and inelastic neutron scattering study of H2 in zeolite, J. Low Temp. Phys. 116 (1999) 149–165, https://doi.org/10.1023/A:1021881516198.
[27] T. Thomberg, A. Jänes, E. Lust, Energy and power performance of electrochemical double-layer capacitors based on molybdenum carbide derived carbon, Electrochim. Acta 55 (9) (2010) 3138–3143, https://doi.org/10.1016/j.electacta.2010.01.075.
[28] E. Härk, et al., Impact of the various catalysts (Pt, Pt-Ru) deposited onto carbon support to the slow oxygen reduction reaction kinetics, ECS Trans. 45 (21) (2013) 1–11, https://doi.org/10.1149/04521.0001ecst.
[29] T. Thomberg, A. Jänes, E. Lust, Energy and power performance of vanadium carbide derived carbon electrode materials for supercapacitors, J. Electroanal. Chem. 630 (1–2) (2009) 55–62, https://doi.org/10.1016/j.jelechem.2009.02.015.
[30] T. Tooming, T. Thomberg, H. Kurig, A. Jänes, E. Lust, High power density supercapacitors based on the carbon dioxide activated d-glucose derived carbon electrodes and 1-ethyl-3-methylimidazolium tetrafluoroborate ionic liquid, J. Power Sources 280 (2015) 667–677, https://doi.org/10.1016/j.jpowsour.2015.01.157.
[31] L. Naheed, et al., Hydrogen adsorption properties of carbide-derived carbons at ambient temperature and high pressure, Int. J. Hydrogen Energy 46 (29) (2021) 15761–15772, https://doi.org/10.1016/j.ijhydene.2021.02.109.
[32] S. Dyjak, W. Kiciński, M. Norek, M. Dyjak, S. Cudziło, Carbide-derived carbon obtained via bromination of titanium carbide: comparative analysis with chlorination and hydrogen storage studies, Microporous Mesoporous Mater. 273 (2019) 26–34, https://doi.org/10.1016/j.micromeso.2018.06.03.
[33] A. Jänes, T. Thomberg, H. Kurig, E. Lust, Nanoscale fine-tuning of porosity of carbide-derived carbon prepared from molybdenum carbide, Carbon 47 (1) (2009) 23–29, https://doi.org/10.1016/j.carbon.2008.07.010.
[34] A. Lewandowski, M. Galinski, Practical and theoretical limits for electrochemical double-layer capacitors, J. Power Sources 173 (2) (2007) 822–828, https://doi.org/10.1016/j.jpowsour.2007.05.062.
[35] E. Tee, I. Tallo, H. Kurig, T. Thomberg, A. Jänes, E. Lust, Huge enhancement of energy storage capacity and power density of supercapacitors based on the carbon dioxide activated microporous SiC-CDC, Electrochim. Acta 161 (2015) 364–370, https://doi.org/10.1016/j.electacta.2015.02.106.
[36] I. Tallo, T. Thomberg, K. Kontturi, A. Jänes, E. Lust, Nanostructured carbide-derived carbon synthesized by chlorination of tungsten carbide, Carbon 49 (13) (2011) 4427–4433, https://doi.org/10.1016/j.carbon.2011.06.033.
[37] I. Tallo, T. Thomberg, H. Kurig, K. Kontturi, A. Jänes, E. Lust, Novel micromesoporous carbon materials synthesized from tantalum hafnium carbide and tungsten titanium carbide, Carbon 67 (2014) 607–616, https://doi.org/10.1016/j.carbon.2013.10.034.
[38] M. Pohl, H. Kurig, I. Tallo, A. Jänes, E. Lust, Novel sol-gel synthesis route of carbide-derived carbon composites for very high power density supercapacitors, Chem. Eng. J. 320 (2017) 576–587, https://doi.org/10.1016/j.cej.2017.03.081.
[39] V. Presser, M. Heon, Y. Gogotsi, Carbide-derived carbons - from porous networks to nanotubes and graphene, Adv. Funct. Mater. 21 (5) (2011) 810–833, https://doi.org/10.1002/adfm.201002094.
[40] R. Härmas, et al., Carbide-Derived Carbons: WAXS and Raman Spectra for Detailed Structural Analysis," C 7 (1) (2021), https://doi.org/10.3390/c7010029. Art. no. 1.
[41] H. Kurig, M. Russina, I. Tallo, M. Siebenbürger, T. Romann, E. Lust, The suitability of infinite slit-shaped pore model to describe the pores in highly porous carbon materials, Carbon 100 (2016) 617–624, https://doi.org/10.1016/j.carbon.2016.01.061.
[42] R. Palm, et al., Study of the structural curvature in Mo2C derived carbons with contrast matched small-angle neutron scattering, Carbon 171 (2021) 695–703, https://doi.org/10.1016/j.carbon.2020.09.070.
[43] M. Bee, Quasielastic Neutron Scattering, Adam Hilger, United Kingdom, 1988.
[44] M.T.F. Telling, A Practical Guide to Quasi-Elastic Neutron Scattering, Royal Society of Chemistry, 2020.
[45] E. Bahn, et al., Ultra-fast diffusion of hydrogen in a novel mesoporous N-doped carbon, Carbon 166 (2020) 307–315, https://doi.org/10.1016/j.carbon.2020.05.004.
[46] M. Paalo, I. Tallo, T. Thomberg, A. Jänes, E. Lust, Enhanced power performance of highly mesoporous sol-gel TiC derived carbons in ionic liquid and non-aqueous electrolyte based capacitors, J. Electrochem. Soc. 166 (13) (2019) A2887, https://doi.org/10.1149/2.0721913jes.
[47] J. Jagiello, M. Thommes, Comparison of DFT characterization methods based on N2, Ar, CO2, and H2 adsorption applied to carbons with various pore size distributions, Carbon 42 (7) (2004) 1227–1232, https://doi.org/10.1016/j.carbon.2004.01.022.
[48] J. Jagiello, C.O. Ania, J.B. Parra, L. Jagiello, J.J. Pis, Using DFT analysis of adsorption data of multiple gases including H2 for the comprehensive characterization of microporous carbons, Carbon 45 (5) (2007) 1066–1071, https://doi.org/10.1016/j.carbon.2006.12.011.
[49] A. Bianco, H.-M. Cheng, T. Enoki, Y. Gogotsi, R.H. Hurt, N. Koratkar, et al., All in the graphene family – a recommended nomenclature for two-dimensional carbon materials, Carbon 65 (2013) 1–6, https://doi.org/10.1016/j.carbon.2013.08.038.
[50] T. Pfaff, M. Simmermacher, B.M. Smarsly, CarbX : a program for the evaluation of wide-angle X-ray scattering data of non-graphitic carbons, J. Appl. Crystallogr. 51 (1) (2018) 219–229, https://doi.org/10.1107/S1600576718000195.
[51] W. Ruland, B. Smarsly, X-ray scattering of non-graphitic carbon: an improved method of evaluation, J Appl Cryst, J Appl Crystallogr 35 (5) (2002) 624–633, https://doi.org/10.1107/S0021889802011007.
[52] C.J. Carlile, M.A. Adams, The design of the IRIS inelastic neutron spectrometer and improvements to its analysers, Phys. B Condens. Matter 182 (4) (1992) 431–440, https://doi.org/10.1016/0921-4526(92)90047-V.
[53] M.D. Le, et al., Upgrade of the MARI spectrometer at ISIS, Nucl. Instrum. Methods Phys. Res. Sect. A Accel. Spectrom. Detect. Assoc. Equip. 1056 (2023) 168646, https://doi.org/10.1016/j.nima.2023.168646.
[54] J. Jagiello, Stable numerical solution of the adsorption integral equation using splines, Langmuir 10 (8) (1994) 2778–2785, https://doi.org/10.1021/la00020a045.
[55] A. Sadezky, H. Muckenhuber, H. Grothe, R. Niessner, U. Pöschl, Raman microspectroscopy of soot and related carbonaceous materials: spectral analysis and structural information, Carbon 43 (8) (2005) 1731–1742, https://doi.org/10.1016/j.carbon.2005.02.018.
[56] J. Ribeiro-Soares, et al., Structural analysis of polycrystalline graphene systems by Raman spectroscopy, Carbon 95 (2015) 646–652, https://doi.org/10.1016/j.carbon.2015.08.020.
[57] M.A. Pimenta, G. Dresselhaus, M.S. Dresselhaus, L.G. Cançado, A. Jorio, R. Saito, Studying disorder in graphite-based systems by Raman spectroscopy, Phys. Chem. Chem. Phys. 9 (11) (2007) 1276–1290, https://doi.org/10.1039/B613962K.
[58] R. Palm, et al., Mobility of H2 adsorbed in multilayers in sol-gel method TiC derived carbon, STFC ISIS Neutron and Muon Source (2021), https://doi.org/10.5286/ISIS.E.RB2010339.
[59] R. Palm, et al., Presence of Multilayer H2 Adsorption in Micro- and Mesoporous Carbon, STFC ISIS Neutron and Muon Source, 2020, https://doi.org/10.5286/ISIS.E.RB2010603.
[60] O. Arnold, et al., Mantid—data analysis and visualization package for neutron scattering and μ SR experiments, Nucl. Instrum. Methods Phys. Res. Sect. A Accel. Spectrom. Detect. Assoc. Equip. 764 (2014) 156–166, https://doi.org/10.1016/j.nima.2014.07.029.
[61] P.L. Hall, D.K. Ross, Incoherent neutron scattering functions for random jump diffusion in bounded and infinite media, Mol. Phys. 42 (3) (1981) 673–682, https://doi.org/10.1080/00268978100100521.
[62] R. Härmas, et al., The ortho-para transition, confinement and self-diffusion of H2 in three distinct carbide-derived carbons by quasi- and inelastic neutron scattering, EPJ Web Conf. 286 (2023) 05001, https://doi.org/10.1051/epjconf/202328605001.
[63] D.E. O'Reilly, E.M. Peterson, Self-diffusion of liquid hydrogen and deuterium, J. Chem. Phys. 66 (3) (2008) 934–937, https://doi.org/10.1063/1.434001.
[64] O.-E. Haas, J.M. Simon, S. Kjelstrup, A.L. Ramstad, P. Fouquet, Quasi-elastic neutron scattering investigation of the hydrogen surface self-diffusion on polymer

electrolyte membrane fuel cell catalyst support, J. Phys. Chem. C 112 (8) (2008) 3121–3125, https://doi.org/10.1021/jp077715+.
[65] J.S. Arellano, L.M. Molina, A. Rubio, J.A. Alonso, Density functional study of adsorption of molecular hydrogen on graphene layers, J. Chem. Phys. 112 (18) (2000) 8114–8119, https://doi.org/10.1063/1.481411.
[66] I. Cabria, M.J. López, J.A. Alonso, Density functional study of molecular hydrogen coverage on carbon nanotubes, Comput. Mater. Sci. 35 (3) (2006) 238–242, https://doi.org/10.1016/j.commatsci.2004.10.008.
[67] R. Balderas-Xicohténcatl, H.-H. Lin, C. Lurz, et al., Formation of a super-dense hydrogen monolayer on mesoporous silica, Nat. Chem. 14 (2022) 1319–1324, https://doi.org/10.1038/s41557-022-01019-7.
[68] J. Jagiello, J. Kenvin, C.O. Ania, J.B. Parra, A. Celzard, V. Fierro, Exploiting the adsorption of simple gases O2 and H2 with minimal quadrupole moments for the dual gas characterization of nanoporous carbons using 2D-NLDFT models, Carbon 160 (2020) 164–175, https://doi.org/10.1016/j.carbon.2020.01.013.
[69] K.S. Singwi, A. Sjölander, Diffusive motions in water and cold neutron scattering, Phys. Rev. 119 (3) (1960) 863–871, https://doi.org/10.1103/PhysRev.119.863.
[70] C.T. Chudley, R.J. Elliott, Neutron scattering from a liquid on a jump diffusion model, Proc. Phys. Soc. 77 (2) (1961) 353–361, https://doi.org/10.1088/0370-1328/77/2/319.